applied optics

Numerically stable formulation of Mie theory for an emitter close to a sphere

MATT MAJIC AND ERIC C. LE RU*

The MacDiarmid Institute for Advanced Materials and Nanotechnology, School of Chemical and Physical Sciences, Victoria University of Wellington, P.O. Box 600, Wellington 6140, New Zealand
**Corresponding author: eric.leru@vuw.ac.nz*

Received 4 October 2019; revised 17 December 2019; accepted 1 January 2020; posted 3 January 2020 (Doc. ID 379694); published 4 February 2020

Numerical implementations of Mie theory make extensive use of spherical Bessel functions. These functions are, however, known to overflow/underflow (grow too large/small for floating point precision) for orders much larger than the argument. This is not a problem in applications such as plane wave excitation, as the Mie series converge before these numerical problems arise. However, for an emitter close to the surface of a sphere, the scattered field in the vicinity of the sphere is expressed as slowly converging series, with multipoles up to order 1000 required in some cases. These series may be used to calculate experimentally relevant quantities such as the decay rate of an emitter near a sphere. In these cases, overflow/underflow prevents any calculation in double precision using Mie theory, and alternatives are either computationally intensive (e.g., arbitrary precision calculations) or not accurate enough (e.g., the electrostatics approximation). We present here a formulation of Mie theory that overcomes these limitations. Using normalized Bessel functions where the large growth/decay is extracted as a prefactor, we re-express the Mie coefficients for scattering by spheres in a normalized form. These normalized expressions are used to accurately compute the series for the electric field and decay rate of a dipole emitter near a spherical surface, in cases where the Mie coefficients would normally overflow before any degree of accuracy can be obtained.

https://doi.org/10.1364/AO.379694

1. INTRODUCTION

Mie theory is the exact solution to Maxwell's equations for electromagnetic scattering by spherical particles [1,2]. The incident and scattered fields are expressed as series of vector spherical wave functions (VSWFs), and the series coefficients are related through the Mie coefficients, or susceptibilities, Γ_n and Δ_n, where n refers to the multipole order. Most physical properties, such as far-field cross sections or near-field enhancements, are computed from infinite series involving the Mie coefficients, which contain spherical Bessel functions (SBFs) $j_n(x)$, $j_n(sx)$, and spherical Hankel functions $h_n(x)$, where $x = ka$ is the size parameter for sphere radius a and wavenumber k, and s is the relative refractive index (possibly complex). These functions either decrease or increase rapidly with order n for $n \gtrsim x$. The Mie coefficients themselves decrease very rapidly for $n \gtrsim x$, and as a consequence, the series for most physical quantities converge quickly—the maximum multipole order required to converge for plane-wave excitation is n modestly greater than x [3,4].

Numerical implementations of Mie theory may, however, be hampered by overflow/underflow in the computation of the Bessel functions [5]. Overflow/underflow here means the analytical values become greater/less than the largest/smallest storable floating point number. This is on the order of $10^{\pm 308}$ for double precision arithmetic (Float64). For problems involving plane-wave excitation, no overflow occurs unless the particle is large and absorbing, i.e., $\mathrm{Im}\{sx\}$ is large. In this case, the problem can be overcome by re-expressing the Bessel functions in Mie coefficients in terms of ratios of consecutive orders or their logarithmic derivatives [6–8].

But another less documented source of overflow occurs when computing the optical properties of a dipole emitter near the sphere. This generalization of Mie theory provides in particular a means to calculate the total decay rate of the emitter through evaluating the reflected field at the dipole position [9]. This is relevant to a number of experimental techniques, including surface-enhanced fluorescence and Raman spectroscopy [10–13], the study of strong coupling of dye molecules on plasmonic nanoparticles [14–16], or Mie resonances in dielectric particles [17]. The dipole Mie solution involves a series of Mie coefficients, but unlike for plane-wave excitation, the series converge slowly when the distance to the surface is small compared to the sphere radius [13,18], requiring multipole orders up to 1000 to reach adequate accuracy. As we will show, the

decay rates cannot be accurately computed over a large range of parameters, notably for dipole distances d small compared to the sphere radius a, typically $d/a < 20$. This encompasses a number of experimentally relevant situations such as a fluorophore adsorbed 1 nm from the surface of a 40–100 nm diameter nanoparticle, or any emitter (such as a dye or quantum dot) attached to a dielectric microsphere. In such cases, overflow will prevent any calculations of decay rate or scattered field in the vicinity of the sphere using Mie theory. As an alternative, many researchers turn to the quasistatic approximation, where overflow does not occur, and this slow convergence can also be overcome using more efficient formulations based on image theory [19–25]. However, the quasistatic limit is only a rough approximation, and these image formulations cannot be easily extended to Mie theory.

This work aims to overcome this limitation. To this end, we develop an improved implementation of Mie theory that is less prone to overflow. We apply it to the case of a dipolar emitter close to a sphere and show that optical properties can be computed over a much larger range of relevant parameters in double precision arithmetic. Central to our approach is the use of "normalized SBFs" $\bar{j}_n(x)$, $\bar{y}_n(x)$, which are simply the SBFs multiplied by suitable factors so that they remain of order 1 for large n. These were proposed in Refs. [26–28], but despite their simplicity, they have not to our knowledge been used within Mie theory.

2. NORMALIZED SPHERICAL BESSEL FUNCTIONS

For large n, the SBFs $j_n(x)$ decrease quickly with order while $y_n(x)$ increase with order. This causes underflow/overflow where the numerical values are stored as either 0, $\pm\infty$, or NaN. If high orders are desired, one can separate out analytically the simple prefactor that governs this large n behavior and calculate the remaining factor as done in Ref. [26]. In this section, we present the main features of these normalized SBFs before incorporating them into Mie theory. They may be defined according to Ref. [26] as

$$\bar{j}_n(x) = \frac{(2n+1)!!}{x^n} j_n(x), \tag{1}$$

$$\bar{y}_n(x) = \frac{-x^{n+1}}{(2n-1)!!} y_n(x), \tag{2}$$

$$\bar{h}_n(x) = \frac{ix^{n+1}}{(2n-1)!!} h_n(x), \tag{3}$$

$$= \frac{ix^{2n+1}}{(2n+1)!!(2n-1)!!} \bar{j}_n(x) + \bar{y}_n(x). \tag{4}$$

$h_n(x) = j_n(x) + iy_n(x)$ is the spherical Hankel function of the first kind. These are normalized so that,

$$\bar{j}_{n\to\infty} \sim \bar{y}_{n\to\infty} \sim \bar{h}_{n\to\infty} \sim 1 + \mathcal{O}(1/n).$$

Note that the Bessel functions are related through $j_n(x) = y_{-n-1}(x)$, and similarly, we have $\bar{j}_n(x) = \bar{y}_{-n-1}(x)$, reflecting their inverse behavior with respect to n. Since the reason for using these normalized functions is to avoid overflow/underflow, we cannot use Eqs. (1)–(3) to calculate them. We could use normalized series expressions based off explicit expressions for the SBFs [29], but they converge quickly only for small x. Instead, we propose to compute the normalized Bessel functions from their recurrence relations, which are similar to those of the SBFs [26]:

$$\bar{j}_{n+1} = \frac{4(n+1)^2 - 1}{x^2}(\bar{j}_n - \bar{j}_{n-1}), \tag{5}$$

$$\bar{y}_{n+1} = \bar{y}_n - \frac{x^2}{4n^2-1}\bar{y}_{n-1}, \tag{6}$$

$$\bar{h}_{n+1} = \bar{h}_n - \frac{x^2}{4n^2-1}\bar{h}_{n-1}, \tag{7}$$

with initial values

$$\bar{j}_0 = \frac{\sin x}{x}, \quad \bar{j}_1 = \frac{3}{x^2}\left(\frac{\sin x}{x} + \cos x\right), \tag{8}$$

$$\bar{y}_0 = \cos x, \quad \bar{y}_1 = x\sin x - \cos x, \tag{9}$$

$$\bar{h}_0 = e^{ix}, \quad \bar{h}_1 = e^{ix}(1-ix). \tag{10}$$

The recurrence [Eq. (5)] for $\bar{j}_n$ is unstable in the upward direction (increasing n), so a downward recurrence implementation should be used instead, just as is done for the standard Bessel functions j_n [2] (see Appendix A for details). $\bar{y}_n(x)$ and $\bar{h}_n(x)$ can be computed by standard forward recurrence without numerical problems, except for x with a large imaginary part (see Appendix B for details). None of the series considered in this paper contains $\bar{y}_n(x)$ of a complex argument, but this could be a problem if considering layered spheres.

The behaviors of the normalized SBFs are plotted alongside the standard spherical Bessel functions in Fig. 1. For x real and $n < x$, the SBFs are roughly constant with n, while the normalized functions behave as either $(2n+1)!!/x^n$ or $x^{n+1}/(2n-1)!!$, reaching a maximum or minimum value at $n \approx x/2$, and then tend towards 1. $\bar{y}_n(x)$ and $\bar{j}_n(x)$ are safe from overflow/underflow for real $x \lesssim 1400$. For $x = 1400$, the normalized Bessel functions nearly overflow at $n \approx 700$. For x complex, both the standard and normalized Bessel functions start at $n = 0$ with a large absolute value, which can lead to overflow for all orders. This is seen, for example, in Fig. 1(b) for $x = 700i$. This situation is relevant for large strongly dissipative spheres, and can be avoided by calculating ratios of consecutive orders or logarithmic derivatives [6–8].

The advantage of these functions is that the simple prefactors simplify in products and fractions of SBFs. This allows the computation of products such as $h_n(x)\,j_n(y)$ up to high orders with $n \gg x, y$, which we shall demonstrate in the context of Mie theory.

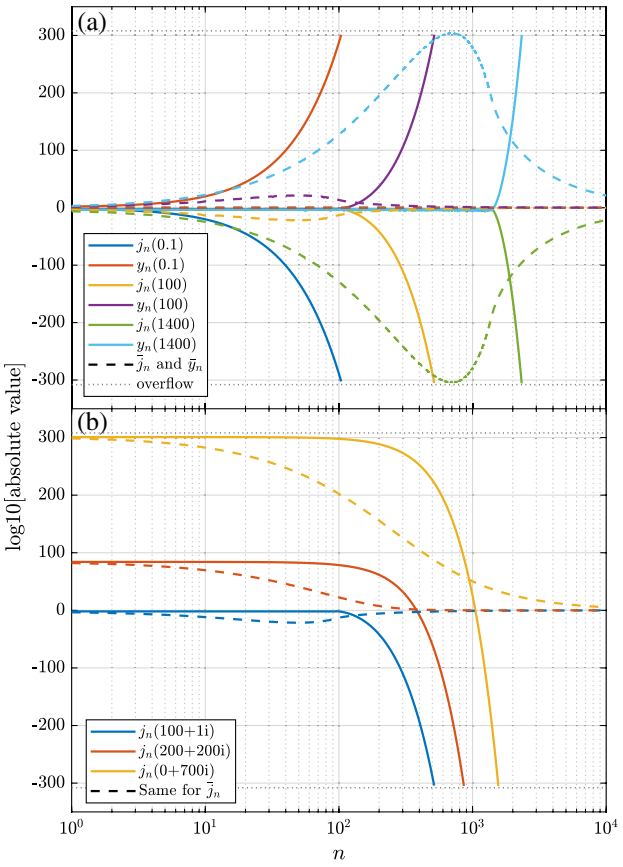

Fig. 1. Plots of standard (solid lines) and normalized (dashed lines) spherical Bessel functions for (a) real and (b) complex arguments. $\bar{y}_n(x)$ are computed by forward recurrence and $\bar{j}_n(x)$ by backward recurrence. We do not show $\bar{y}_n$ in (b), as it does not appear with a complex argument in our analysis.

3. NORMALIZED SUSCEPTIBILITIES OF A SPHERE

For a sphere of radius a and relative permittivity ϵ_s in a medium of relative permittivity ϵ_m, excited by a time harmonic electromagnetic field of wavelength λ and wavenumber $k = 2\pi\sqrt{\epsilon_m}/\lambda$, the Mie coefficients of a sphere are given by [13]

$$\Delta_n = -\frac{\psi_n'(s\,x)\psi_n(x) - s\,\psi_n(s\,x)\psi_n'(x)}{\psi_n'(s\,x)\xi_n(x) - s\,\psi_n(s\,x)\xi_n'(x)}, \tag{11}$$

$$\Gamma_n = -\frac{s\,\psi_n'(s\,x)\psi_n(x) - \psi_n(s\,x)\psi_n'(x)}{s\,\psi_n'(s\,x)\xi_n(x) - \psi_n(s\,x)\xi_n'(x)}, \tag{12}$$

where $x = ka$ is the size parameter, $s = \sqrt{\epsilon_s}/\sqrt{\epsilon_m}$ is the relative refractive index, and $\psi_n(x) = x\,j_n(x)$ and $\xi_n(x) = x\,h_n(x)$ are the Riccati–Bessel functions, with $'$ denoting their derivative.

These susceptibilities suffer from two possible sources of overflow/underflow. First, if $s\,x$ has a large imaginary part, the Bessel functions become exponentially large, as pointed out in the previous section. This source of overflow is known to be avoided by instead computing the logarithmic derivatives of the Riccati–Bessel functions [8]:

$$\Delta_n = -\frac{j_n(x)}{h_n(x)}\frac{A_n(s\,x) - s\,A_n(x)}{A_n(s\,x) - s\,B_n(x)}, \tag{13}$$

$$\Gamma_n = -\frac{j_n(x)}{h_n(x)}\frac{s\,A_n(s\,x) - A_n(x)}{s\,A_n(s\,x) - B_n(x)}, \tag{14}$$

where A_n and B_n are logarithmic derivatives of the unnormalized Riccati–Bessel functions:

$$A_n(x) = \frac{\psi_n'(x)}{\psi_n(x)}, \quad B_n(x) = \frac{\xi_n'(x)}{\xi_n(x)}, \tag{15}$$

which may be calculated via a continued fraction recurrence. For numerical stability, A_n should be calculated via backward recurrence, and B_n via forward recurrence [8]:

$$A_{n-1} = \frac{n}{x} - \frac{1}{\frac{n}{x} + A_n}, \tag{16}$$

$$B_n = -\frac{n}{x} + \frac{1}{\frac{n}{x} - B_{n-1}}. \tag{17}$$

This implementation avoids issues with large complex $s\,x$, since we still have $A_n(s\,x) \sim \mathcal{O}(1)$ for all orders.

The other source of overflow, which is more pertinent for small scatterers and point sources that we deal with here, occurs for $n \gg x$, where Γ_n and Δ_n decrease quickly with n. This behavior is due to the factors j_n/h_n in Eqs. (13) and (14), decreasing at twice the rate of the Bessel functions individually. To work around this, the leading dependence can be separated out:

$$\Delta_n = \frac{i(2n+1)x^{2n+1}}{(2n+1)!!^2}\bar{\Delta}_n, \tag{18}$$

$$\Gamma_n = \frac{i(2n+1)x^{2n+1}}{(2n+1)!!^2}\bar{\Gamma}_n, \tag{19}$$

where we have defined normalized Mie coefficients:

$$\bar{\Delta}_n = -\frac{\bar{j}_n(x)}{\bar{h}_n(x)}\frac{A_n(s\,x) - s\,A_n(x)}{A_n(s\,x) - s\,B_n(x)}, \tag{20}$$

$$\bar{\Gamma}_n = -\frac{\bar{j}_n(x)}{\bar{h}_n(x)}\frac{s\,A_n(s\,x) - A_n(x)}{s\,A_n(s\,x) - B_n(x)}. \tag{21}$$

Expressions similar to Eqs. (18) and (19) were recognized in Ref. [30] but as an approximation for the location of Mie resonances for small spheres.

The large n limit of $\bar{\Delta}_n$ and $\bar{\Gamma}_n$ is

$$\bar{\Delta}_{n\to\infty} = \frac{s^2-1}{s^2+1}, \quad \bar{\Gamma}_{n\to\infty} = \frac{x^2(s^2-1)}{(2n+1)(2n+3)}. \tag{22}$$

These normalized susceptibilities can therefore be computed to arbitrarily high orders (as long as $x \lesssim 700$—for an extension to larger spheres, see Appendix C), in contrast to Δ_n and Γ_n, which underflow for reasonably small n, as shown in Fig. 2.

We have checked the numerical accuracy of the normalized susceptibilities by computing the relative error of Eqs. (11) and (12) versus Eqs. (18) and (19). Errors were below 10^{-10} for most size parameters x and materials s considered here, for all n up to the highest computable order before overflow of Δ_n and Γ_n.

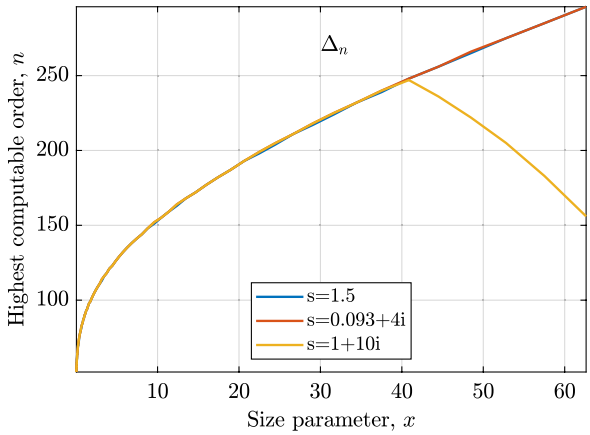

Fig. 2. Maximum order n that can be computed for the unnormalized electric susceptibility Δ_n as computed via Eq. (11) for spheres of different sized parameter x at $\lambda = 633$ nm for typical refractive indices s: dielectric, metallic, and a strongly absorbing material. Results are virtually identical in the first two cases, but for the last case, the series breaks down sooner as $\mathrm{Im}\{s\,x\}$ is large—these issues can be avoided by instead using logarithmic derivatives as in Eq. (13). Results for Γ_n are similar.

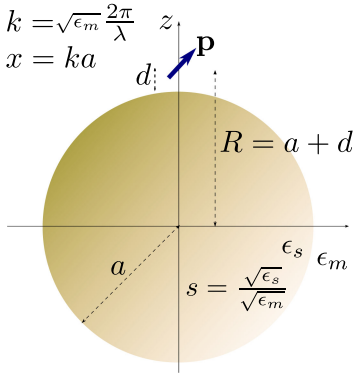

Fig. 3. Schematic of the problem with main parameters and notations: a dipole emitter is located on the z axis at a distance d from a sphere of radius a with relative refractive index s. $x = ka$ is the size parameter.

4. DIPOLE EMITTER NEAR A SPHERE

As the main application of these functions, we consider a radiating electric dipole $\mathbf{p}$ located outside the sphere on the z axis at $z = R$, as depicted in Fig. 3. We follow the standard treatment of this case within Mie theory [9,13], but adapt it to exploit normalized SBFs.

A. Dipole Perpendicular to Surface

First we analyze the perpendicular case where $\mathbf{p} = p\hat{\mathbf{z}}$. The electric field of the dipole can be expressed as a VSWF:

$$\mathbf{E}_i^{\perp} = E_0 \mathbf{N}_1(k\mathbf{r}_p), \quad \text{where} \quad E_0 = \frac{ik^3 p}{4\pi\epsilon_m}. \tag{23}$$

$\mathbf{r}_p$ is the vector extending from the dipole position to the observation point $\mathbf{r}$, and $\mathbf{N}_1(k\mathbf{r}_p) = \frac{1}{k}\nabla\times\nabla\times[\mathbf{r}_p h_1(kr_p)\cos\theta_p]$.

To solve for the scattered field using Mie theory, the incident field must be expanded as a series of spherical wavefunctions centered at the origin:

$$\mathbf{E}_i^{\perp} = \frac{E_0}{kR}\sum_{n=1}^{\infty}(2n+1)h_n(kR)\mathbf{n}_n(k\mathbf{r}), \qquad r < R, \tag{24}$$

where $\mathbf{n}_n(k\mathbf{r}) = \frac{1}{k}\nabla\times\nabla\times[\mathbf{r}\,j_n(kr)P_n(\cos\theta)]$ and $\mathbf{N}_n(k\mathbf{r}) = \frac{1}{k}\nabla\times\nabla\times[\mathbf{r}h_n(kr)P_n(\cos\theta)]$ are the interior and exterior VSWFs defined following Stratton [31] (see Appendix D for a summary of VSWF definitions). The scattered field can then be deduced from Mie theory:

$$\mathbf{E}_s^{\perp} = \frac{E_0}{kR}\sum_{n=1}^{\infty}(2n+1)\Delta_n h_n(kR)\mathbf{N}_n(k\mathbf{r}). \tag{25}$$

Noting the explicit expression for the VSWFs,

$$\mathbf{N}_n(k\mathbf{r}) = n(n+1)\frac{h_n(kr)}{kr}P_n^m(\cos\theta)\hat{\mathbf{r}} + \frac{\xi_n'(kr)}{kr}\frac{\mathrm{d}P_n(\cos\theta)}{\mathrm{d}\theta}\hat{\theta}, \tag{26}$$

we see that the series for the scattered fields contain the problematic products $\Delta_n h_n(kR)h_n(kr)$ and $\Delta_n h_n(kR)\xi_n'(kr)$, which result in slow convergence when $r \approx a \approx R$ and are still susceptible to overflow. Hence, we define normalized VSWFs:

$$\bar{\mathbf{N}}_n(k\mathbf{r}) = \frac{i(kr)^{n+1}}{(2n-1)!!}\mathbf{N}_n(k\mathbf{r}). \tag{27}$$

The vector components of $\bar{\mathbf{N}}_n$ can be obtained simply from the non-normalized functions by replacing the Bessel functions with their normalized versions: $h_n \to \bar{h}_n$ and $\xi_n' \to \hat{\xi}_n$, where

$$\hat{\xi}_n(x) \equiv \frac{ix^{n+1}\xi_n'(x)}{(2n-1)!!} = (n+1)\bar{h}_n(x) - (2n+1)\bar{h}_{n+1}(x). \tag{28}$$

We can then rewrite the series for the scattered field in normalized form:

$$\mathbf{E}_s^{\perp} = \frac{E_0}{k^2 a R}\sum_{n=1}^{\infty}\left(\frac{R}{r}\right)^{n+1}\bar{\Delta}_n\bar{h}_n(kR)\bar{\mathbf{N}}_n(k\mathbf{r}), \tag{29}$$

This expression avoids overflow in the series coefficients and therefore allows computation up to high orders, which is necessary when evaluating the scattered field near the sphere if the dipole is close to the surface.

B. Parallel Dipole

For completeness, we present the same analysis for a dipole parallel to the surface with moment $\mathbf{p} = p\hat{\mathbf{x}}$. Again, the dipole field should be expanded as a multipole series at the origin. Before, the expansion of the perpendicular dipole had only electric multipoles due to the fact that the magnetic field has only a ϕ component, but for the parallel dipole, the expansion must include wave functions of both the electric and magnetic type [9]:

$$E_i^{||} = E_0 \mathbf{N}_{11}^c(\mathbf{r}_p) = E_0 \sum_{n=1}^{\infty} \frac{2n+1}{n(n+1)} \times \left[\frac{\xi_n'(kR)}{kR} \mathbf{n}_{n1}^c(k\mathbf{r}) + h_n(kR)\mathbf{m}_{n1}^s(k\mathbf{r}) \right]_{r<R}, \quad (30)$$

where $\mathbf{N}_{11}^c(k\mathbf{r}_p)$, $\mathbf{n}_{n1}^c(k\mathbf{r})$, and $\mathbf{m}_{n1}^s(k\mathbf{r})$ are defined in Appendix D. The solution to the scattered field expressed in both unnormalized and normalized forms is

$$\mathbf{E}_s^{||} = E_0 \sum_{n=1}^{\infty} \frac{2n+1}{n(n+1)} \times \left[\Delta_n \frac{\xi_n'(kR)}{kR} \mathbf{N}_{n1}^c(\mathbf{r}) + \Gamma_n h_n(kR)\mathbf{M}_{n1}^s(\mathbf{r}) \right] \quad (31)$$

$$= E_0 \sum_{n=1}^{\infty} \frac{1}{n(n+1)} \left(\frac{R}{r}\right)^{n+1} \times \left[\bar{\Delta}_n \frac{\hat{\xi}_n(kR)}{k^2 a R} \bar{\mathbf{N}}_{n1}^c(\mathbf{r}) + \frac{\bar{\Gamma}_n}{ka} \bar{h}_n(kR)\bar{\mathbf{M}}_{n1}^s(\mathbf{r}) \right], \quad (32)$$

where $\bar{\mathbf{N}}_{n1}^c$ and $\bar{\mathbf{M}}_{n1}^s$ are defined the same way as in Eq. (27).

C. Decay Rate Modification Factors

One of the most important applications of Mie theory for dipolar emitters is to compute the radiative (M_{rad}) and total (M_{tot}) decay rate modification factors for emitters such as fluorophores in the vicinity of a sphere. For example, the total decay rate modification factor of a dipole emitter near a scatterer, compared to the same dipole embedded in the same medium without the sphere, is obtained from Refs. [9,13]

$$M_{\text{tot}} = 1 + \frac{6\pi\epsilon_0\epsilon_m}{k^3|p|^2} \text{Im}\left\{\mathbf{p}\cdot\mathbf{E}_s(\mathbf{r}_p)\right\}, \quad (33)$$

which involves the series Eqs. (25) and (31) evaluated at the source location. For both dipole orientations, the standard series solutions and their normalized equivalent are given below, with $X = kR$:

$$M_{\text{tot}}^{\perp} = 1 + \frac{3}{2X^2} \sum_{n=1}^{\infty} (2n+1)(n+1)n \text{Re}\left\{\Delta_n h_n(X)^2\right\} \quad (34)$$

$$= 1 + \frac{3}{2X^3} \sum_{n=1}^{\infty} (n+1)n \left(\frac{a}{R}\right)^{2n+1} \text{Im}\left\{\bar{\Delta}_n \bar{h}_n(X)^2\right\}, \quad (35)$$

$$M_{\text{tot}}^{||} = 1 + \frac{3}{4X^2} \sum_{n=1}^{\infty} (2n+1) \text{Re}\left\{\Delta_n \xi_n'(X)^2 + \Gamma_n \xi_n(X)^2\right\} \quad (36)$$

$$= 1 + \frac{3}{4} \sum_{n=1}^{\infty} \left(\frac{a}{R}\right)^{2n+1} \text{Im}\left\{\bar{\Delta}_n \frac{\hat{\xi}_n(X)^2}{X^3} + \bar{\Gamma}_n \frac{\bar{h}_n(X)^2}{X}\right\}. \quad (37)$$

For the purpose of Fig. 4, we present these decay rates in the electrostatic limit:

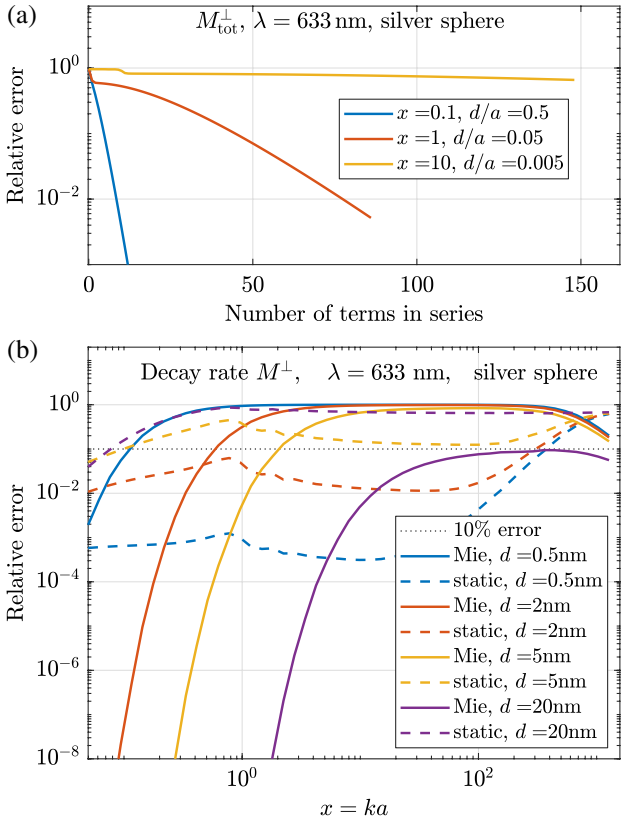

Fig. 4. (a) Relative errors as a function of maximum multipole order of the standard Mie theory series [9] for the decay rate modification $M_{\text{tot}}^{\perp}$ of a dipole perpendicular to the surface of a silver sphere at $\lambda = 633$ nm ($s = 0.093 + 4i$). d is fixed at 5 nm with $a = 10$, 100, or 1000 nm. The curves stop when overflow occurs (in double precision). (b) Summary of the minimum error obtainable from the same series computed up to its point of overflow as a function of size parameter for different d. Sphere radii for these x values range from $a = 5$ nm to 160 μm, where both Mie series [Eqs. (34), (35)] break down. The results for the equivalent electrostatics problem are also shown.

$$M_{\text{tot}}^{\perp} \approx 1 + \frac{3}{2X^3} \sum_{n=1}^{\infty} (n+1)^2 \text{Im}\left\{\frac{\epsilon - 1}{n(\epsilon+1)+1}\right\} \left(\frac{a}{R}\right)^{2n+1}, \quad (38)$$

$$M_{\text{tot}}^{||} \approx 1 + \frac{3}{4X^3} \sum_{n=1}^{\infty} n(n+1) \text{Im}\left\{\frac{\epsilon - 1}{n(\epsilon+1)+1}\right\} \left(\frac{a}{R}\right)^{2n+1}. \quad (39)$$

As for the scattered field, these series [Eqs. (34)–(39)] converge slowly when the dipole is close to the sphere at a distance $d \ll a$.

Overflow errors are therefore a serious limitation to compute dipolar decay rates with the unnormalized implementation. This is illustrated in Fig. 4, which shows the relative errors in computing the total decay rate of a radially oriented dipole near a sphere from the standard approach, Eq. (34), with as many terms in the series as possible before overflow occurs. It clearly shows that satisfactory errors cannot be obtained over a large range of parameters, notably for dipole distances d small compared to the sphere radius a, typically $d/a < 20$. As shown

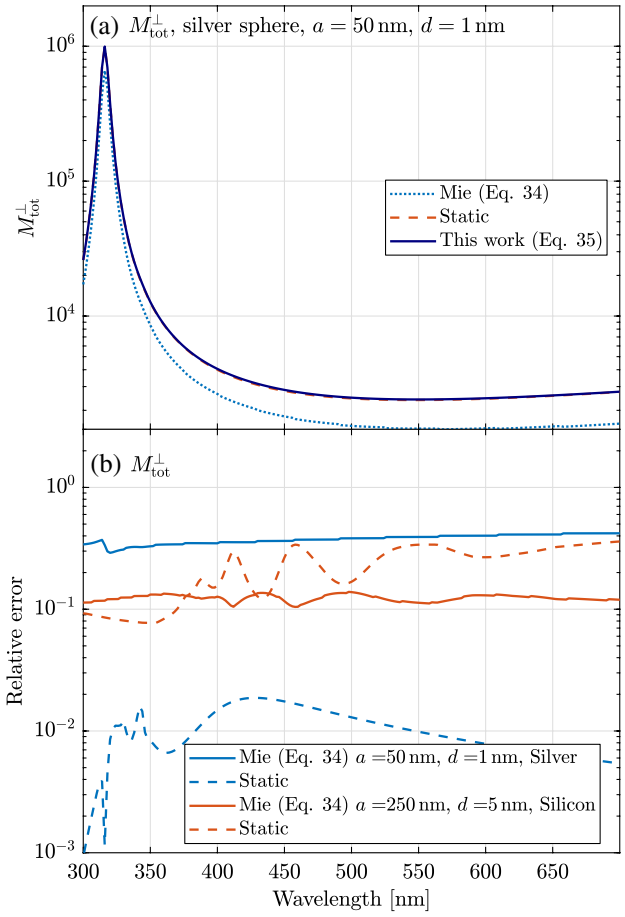

Fig. 5. (a) Spectral dependence of the total decay rate modification factor $M_{\rm tot}^{\perp}$ for a typical scenario of a perpendicular dipole $d = 1$ nm from an $a = 50$ nm radius silver sphere in air. The dielectric function is taken from Ref. [34]. Three calculations are considered: standard Mie theory [Eq. (34)] using as many terms as possible without overflow, the electrostatics approximation with 2000 terms (this is more than needed for full convergence in double precision), and the normalized approach [Eq. (35)] with 2000 terms. The corresponding relative errors (compared to the normalized approach) are shown in (b) for the same case, and for comparison, also for $d = 5$ nm nm and an $a = 250$ nm radius silicon sphere.

in Fig. 4(b), the electrostatics approximation [Eq. (38)] may provide a reasonable alternative, but fails when the dipole is moved away from the surface, even by as little as 2 nm. In some situations, neither Mie theory nor the electrostatics approximation provides an estimate with better than 10% relative error. In contrast, the normalized series, Eq. (35), can be computed to any degree of accuracy in all cases.

This provides a relatively simple means to accurately compute, for example, the spectral dependence of the total decay rate of an emitter adsorbed on a metallic sphere, an important quantity in the context of surface-enhanced fluorescence [32,33], as shown explicitly in Fig. 5.

We note that for very large spheres with $700 \lesssim x \lesssim 1800$, $M_{\rm tot}$ was computed using a combination of the unnormalized and normalized expressions—Eqs. (34), (36) for $n \lesssim x$, and Eqs. (35), (37) for $n \gtrsim x$. See Appendix C for details.

Finally, we point out that for non-absorbing materials, s is real, and this leads to severely inaccurate calculations of $\mathrm{Re}\{\Delta_n h_n (kR)^2\}$ (which is then much smaller than $\mathrm{Im}\{\bar{\Delta}_n \bar{h}_n (kR)^2\}$) in all implementations considered here. However, in this case, $M_{\rm tot} = M_{\rm rad}$, where the series for $M_{\rm rad}$ [13] does not have this problem and does not suffer from the same slow convergence so may be computed using the unnormalized implementation.

5. CONCLUSION AND OUTLOOK

A stable implementation of generalized Mie theory for dipolar emitters has been proposed and demonstrated. It enables accurate double-precision computations for arbitrarily close emitters over a large range of size parameters x, in particular for typical nanoscale geometries encountered in plasmonics where the standard implementation cannot reach any degree of accuracy. It provides in particular an accurate numerical estimate of the modification of the decay rates for emitters near a sphere. This can be applied, for example, to study surface-enhanced fluorescence for fluorophores adsorbed on or very close to metallic nanoparticles. The proposed method is straightforward to implement and no more computationally intensive than the standard approach.

Mie coefficients for layered spheres behave similarly to those for solid spheres, as $n \to \infty$. Hence, there is no problem of overflow for plane-wave excitation (unless the sphere is large and strongly absorbing), but the same overflow problem occurs for emitters close to layered spheres, as considered in Ref. [35]. The approach here should be straightforward to extend to multilayered spheres, since the multilayer Mie coefficients are expressed in terms of the single-layer coefficients Δ_n, Γ_n along with SBFs j_n, h_n [36]. The specific problem treated here can be seen as stemming from the translation relations for spherical wave functions, since the translation coefficients contain similar products of Bessel functions, making overflow a problem near the radius of divergence. The T-matrix is in effect a generalization of the Mie coefficients (which form its diagonal). The same problems of overflow arise for emitters close to the surface, so a similar normalized implementation of the T-matrix should resolve this problem.

APPENDIX A: BACKWARD RECURRENCE FOR $\bar{j}_n(x)$, $A_n(x)$

Although the forward recurrence for $\bar{j}_n(x)$ is stable until $n \approx x$, the error then grows suddenly. As for $j_n(x)$, in order to accurately compute $\bar{j}_n(x)$ for all n, a backward recurrence must therefore be used. This consists of starting the recurrence at N, the largest order required, with initial values $\bar{j}_N$ and $\bar{j}_{N-1}$, and using Eq. (5) to deduce $\bar{j}_{N-2}$, etc., down to $\bar{j}_0$. $\bar{j}_N$ should be taken initially as an arbitrary very small number to avoid overflow, e.g., 10^{-300}. The modified Lentz algorithm (see Refs. [37, chap. 5.2] and [28]) is used to accurately calculate the ratio $\bar{r} = \bar{j}_N / \bar{j}_{N-1}$ and deduce $\bar{j}_{N-1}$. Once the backward recurrence has been completed, all $\bar{j}_n$ can then be correctly scaled knowing that $\bar{j}_0 = \sin(x)/x$.

Note that, as demonstrated in Ref. [27], an alternative algorithm consists of simply setting $\bar{r} = 1$ and relying on the fact that

the error in $\bar{j}_n$ diminishes as the backward recurrence is iterated. Naturally the recursion should then be initiated for some $n > N$ so that the error is negligible for all $n \le N$. An estimate for the increase in accuracy in each step for $n \gg x$ is $\bar{\epsilon}_n = x^6/(16n^4)$ [27]. Hence, letting α denote the number of extra orders above N that is necessary for all $\bar{j}_n$ to be accurate to within 10^{-15}, we can estimate α from the equation $(\bar{\epsilon}_N)^\alpha = 10^{-15}$.

A similar backward recurrence algorithm for $A_n(x)$ may be used; for more details, see Ref. [8].

For convenience, basic MATLAB codes to evaluate these functions are provided in Code 1, Ref. [38].

APPENDIX B: ERROR IN $\bar{y}_n(x)$ FOR LARGE x COMPLEX

To check the accuracy of the normalized implementation, the Bessel functions were computed via both standard MATLAB codes and custom codes for the normalized Bessel functions, which were multiplied by the prefactors in Eqs. (1) and (2). The errors are low $\lesssim 10^{-13}$ in all cases considered here—$j_n(x)$ and $y_n(x)$ for real x—so we do not plot them, but errors are found for $y_n(x)$ where $\mathrm{Im}\{x\} \gg 1$, which arise in absorbing media or layered spheres, and are plotted in Fig. 6.

APPENDIX C. EXTENSION FOR LARGER SPHERES

For $x \gtrsim 700$, the factor $\bar{h}_n(x)/\bar{j}_n(x)$ in Eqs. (20) and (21) overflows at $n \approx x/2$, but is still computable for $n \to \infty$, while $h_n(x)/j_n(x)$ is computable for $n \lesssim x$ and overflows for $n \gtrsim x$. Therefore, for large x, one should use these functions in the ranges of n for which they are closest to $\mathcal{O}(1)$. The optimum division of these two ranges of n occurs where $h_n(x) = \bar{h}_n(x)$, which occurs roughly at $n = \mathrm{floor}(4x/3)$. In order to compute the normalized Bessel functions in this range, the same recurrences [Eqs. (5), (7)] can be used but with initial values $n = \mathrm{floor}(4x/3)$, which can be obtained from the unnormalized Bessel functions. But even this extension has limitations, since for $x \gtrapprox 1800$, neither the normalized or unnormalized Bessel functions are computable for orders near $n \gtrsim x$. Beyond this,

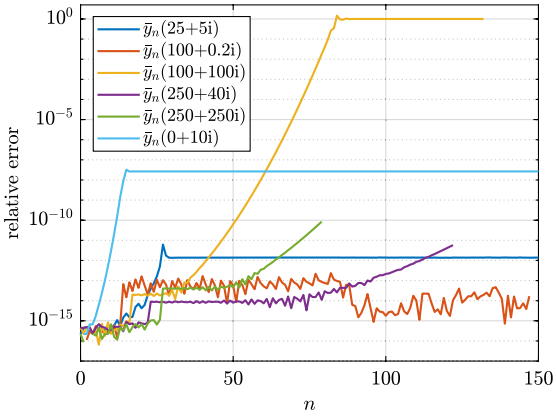

Fig. 6. Relative error in computing $\bar{y}_n(x)$ via forward recursion compared to the MATLAB function Bessel-scaled by $-x^{n+1}/(2n-1)!!$.

perhaps a more refined type of normalization could be introduced. The specific product $h_n(X)^2 j_n(x)/h_n(x)$ in computing the decay rates is itself well behaved for large x, X, so ideally, we should use some method to compute the entire product without having to compute the factors individually. But this is not of great concern since for large spheres, the solution may be well approximated by either a flat planar surface if $d \ll a$, or geometric optics if both $x \gg 1$ and $X \ll 1$.

APPENDIX D: VECTOR SPHERICAL WAVE FUNCTIONS

We use VSWFs identical to Stratton [31]:

$$\mathbf{M}^c_{nm} = \nabla \times [\mathbf{r} h_n(kr) P^m_n(\cos\theta)\cos(m\phi)], \tag{D1}$$

$$\mathbf{N}^c_{nm} = \frac{1}{k}\nabla \times \mathbf{M}^c_{nm}. \tag{D2}$$

These are defined only for $m \ge 0$, and the corresponding functions $\mathbf{M}^s_{nm}$ and $\mathbf{N}^s_{nm}$ are defined with $\sin(m\phi)$ instead of $\cos(m\phi)$. The associated Legendre functions $P^m_n(\cos\theta)$ are here defined without the $(-1)^m$ prefactor. We also use the notation $\mathbf{N}_n \equiv \mathbf{N}^c_{n0}$. The regular VSWFs are denoted with a lower case, e.g., $\mathbf{n}^c_{nm}$, and obtained by using $j_n(kr)$ instead of $h_n(kr)$.

The irregular VSWF components are

$$\begin{matrix}\mathbf{M}^c_{nm} \\ \mathbf{M}^s_{nm}\end{matrix} = h_n(kr)\left(\mp\frac{m}{\sin\theta}P^m_n(\cos\theta)\begin{matrix}\cos \\ \sin\end{matrix} m\phi\hat{\boldsymbol{\theta}} - \frac{\mathrm{d}P^m_n(\cos\theta)}{\mathrm{d}\theta}\begin{matrix}\sin \\ \cos\end{matrix} m\phi\hat{\boldsymbol{\phi}}\right), \tag{D3}$$

$$\begin{matrix}\mathbf{N}^c_{nm} \\ \mathbf{N}^s_{nm}\end{matrix} = n(n+1)\frac{h_n(kr)}{kr}P^m_n(\cos\theta)m\phi\hat{\mathbf{r}}\begin{matrix}\cos \\ \sin\end{matrix} + \frac{\xi_n'(kr)}{kr}\left(\mp\frac{m}{\sin\theta}P^m_n(\cos\theta)\begin{matrix}\sin \\ \cos\end{matrix} m\phi\hat{\boldsymbol{\phi}} + \frac{\mathrm{d}P^m_n(\cos\theta)}{\mathrm{d}\theta}\begin{matrix}\cos \\ \sin\end{matrix} m\phi\hat{\boldsymbol{\theta}}\right). \tag{D4}$$

We note that other VSWF definitions are common. For example, the functions used by Mishchenko [39] are

$$\mathbf{N}_{n0} = \sqrt{\frac{2n+1}{4\pi n(n+1)}}\mathbf{N}_n, \tag{D5}$$

$$\mathbf{N}_{n,m>0} = (-)^m\sqrt{\frac{2n+1}{4\pi n(n+1)}\frac{(n-m)!}{(n+m)!}}\frac{\mathbf{N}^c_{nm} + i\mathbf{N}^s_{nm}}{2}, \tag{D6}$$

and similarly for the other functions $\mathbf{M}_{nm}$, $\mathbf{n}_{nm}$, $\mathbf{m}_{nm}$.

Funding. Marsden Fund (VUW1618).

Acknowledgment. MM thanks Victoria University for support via a VUW doctoral scholarship. ECLR thanks the Royal Society Te Apārangi (New Zealand) for support through a Marsden grant.

Disclosures. The authors declare no conflicts of interest.

REFERENCES

1. G. Mie, "Articles on the optical characteristics of turbid tubes, especially colloidal metal solutions," Ann. Phys. **330**, 377–445 (1908).
2. C. F. Bohren and D. R. Huffman, *Absorption and Scattering of Light by Small Particles* (Wiley, 1983).
3. W. J. Wiscombe, "Improved Mie scattering algorithms," Appl. Opt. **19**, 1505–1509 (1980).
4. J. R. Allardice and E. C. Le Ru, "Convergence of Mie theory series: criteria for far-field and near-field properties," Appl. Opt. **53**, 7224–7229 (2014).
5. A. A. R. Neves and D. Pisignano, "Effect of finite terms on the truncation error of Mie series," Opt. Lett. **37**, 2418–2420 (2012).
6. V. E. Cachorro and L. L. Salcedo, "New improvements for Mie scattering calculations," J. Electromagn. Waves Appl. **5**, 913–926 (1991).
7. J. Shen and X. Cai, "Algorithm of numerical calculation on Lorentz Mie theory," Prog. Electromagn. Res. **1**, 691–694 (2005).
8. C. D. Cantrell, "Numerical methods for the accurate calculation of spherical Bessel functions and the location of Mie resonances," Technical Report EE08-1988 (The University of Texas at Dallas, 2013).
9. H. Chew, "Transition rates of atoms near spherical surfaces," J. Chem. Phys. **87**, 1355–1360 (1987).
10. H. Xu, X. H. Wang, M. P. Persson, H. Q. Xu, M. Käll, and P. Johansson, "Unified treatment of fluorescence and Raman scattering processes near metal surfaces," Phys. Rev. Lett. **93**, 243002 (2004).
11. L. A. Blanco and F. J. García de Abajo, "Spontaneous light emission in complex nanostructures," Phys. Rev. B **69**, 205414 (2004).
12. C. M. Galloway, P. G. Etchegoin, and E. C. Le Ru, "Ultrafast nonradiative decay rates on metallic surfaces by comparing surface-enhanced Raman and fluorescence signals of single molecules," Phys. Rev. Lett. **103**, 063003 (2009).
13. E. C. Le Ru and P. G. Etchegoin, *Principles of Surface Enhanced Raman Spectroscopy and Related Plasmonic Effects* (Elsevier, 2009).
14. H. Mertens, A. F. Koenderink, and A. Polman, "Plasmon-enhanced luminescence near noble-metal nanospheres: comparison of exact theory and an improved Gersten and Nitzan model," Phys. Rev. B **76**, 115123 (2007).
15. R. Chikkaraddy, B. De Nijs, F. Benz, S. J. Barrow, O. A. Scherman, E. Rosta, A. Demetriadou, P. Fox, O. Hess, and J. J. Baumberg, "Single-molecule strong coupling at room temperature in plasmonic nanocavities," Nature **535**, 127 (2016).
16. B. Auguié, B. L. Darby, and E. C. Le Ru, "Electromagnetic interactions of dye molecules surrounding a nanosphere," Nanoscale **11**, 12177–12187 (2019).
17. A. I. Kuznetsov, A. E. Miroshnichenko, M. L. Brongersma, Y. S. Kivshar, and B. Luk'yanchuk, "Optically resonant dielectric nanostructures," Science **354**, aag2472 (2016).
18. A. Moroz, "Superconvergent representation of the Gersten–Nitzan and Ford–Weber nonradiative rates," J. Phys. Chem. C **115**, 19546–19556 (2011).
19. S. Deng and W. Cai, "Extending the fast multipole method for charges inside a dielectric sphere in an ionic solvent: high-order image approximations for reaction fields," J. Comput. Phys **223**, 846–864 (2007).
20. A. Moroz, "Depolarization field of spheroidal particles," J. Opt. Soc. Am. B **26**, 517–527 (2009).
21. J. R. Zurita-Sánchez, "Quasi-static electromagnetic fields created by an electric dipole in the vicinity of a dielectric sphere: method of images," Rev. Mexicana Fis. **55**, 443–449 (2009).
22. P. Linse and L. Lue, "Green's function for a spherical dielectric discontinuity and its application to simulation," J. Chem. Phys. **140**, 044903 (2014).
23. N. Cvetković, M. Stojanović, D. Jovanović, A. Ristić, D. Vučković, and D. Krstić, "Green function of the point source inside/outside spherical domain-approximate solution," in *Engineering Mathematics I*, (Springer, 2016), pp. 79–98.
24. M. Majić, B. Auguié, and E. C. Le Ru, "Spheroidal harmonic expansions for the solution of Laplace's equation for a point source near a sphere," Phys. Rev. E **95**, 033307 (2017).
25. M. Majic and E. C. Le Ru, "A new class of solutions to Laplace equation: regularized multipoles of negative orders," arXiv:1907.11690 (2019).
26. D. M. O'Brien, "Spherical Bessel functions of large order," J. Comput. Phys. **36**, 128–132 (1980).
27. E. Gillman and H. R. Fiebig, "Accurate recursive generation of spherical Bessel and Neumann functions for a large range of indices," Comput. Phys. **2**, 62–72 (1988).
28. A. R. Barnett, "The calculation of spherical Bessel and Coulomb functions," in *Computational Atomic Physics* (Springer, 1996), pp. 181–202.
29. M. Abramowitz and I. A. Stegun, eds., *Handbook of Mathematical Functions* (Dover, 1972).
30. R. Colom, A. Devilez, S. Enoch, B. Stout, and N. Bonod, "Polarizability expressions for predicting resonances in plasmonic and Mie scatterers," Phys. Rev. A **95**, 063833 (2017).
31. J. A. Stratton, *Electromagnetic Theory* (Wiley, 2007).
32. E. C. Le Ru, P. G. Etchegoin, J. Grand, N. Félidj, J. Aubard, and G. Lévi, "Mechanisms of spectral profile modification in SEF," J. Phys. Chem. C **111**, 16076–16079 (2007).
33. R. Gill, L. Tian, W. R. C. Somerville, E. C. Le Ru, H. Van Amerongen, and V. Subramaniam, "Silver nanoparticle aggregates as highly efficient plasmonic antennas for fluorescence enhancement," J. Phys. Chem. C **116**, 16687–16693 (2012).
34. P. G. Etchegoin, E. C. Le Ru, and M. Meyer, "An analytic model for the optical properties of gold," J. Chem. Phys. **125**, 164705 (2006).
35. S. J. Norton and T. Vo-Dinh, "Plasmonics quenching and enhancement of a fluorescing molecule outside and inside a silver metallic nanoshell," IEEE Trans. Nanotechnol. **10**, 1264–1274 (2011).
36. D. Schebarchov, B. Auguié, and E. C. Le Ru, "Simple accurate approximations for the optical properties of metallic nanospheres and nanoshells," Phys. Chem. Chem. Phys. **15**, 4233–4242 (2013).
37. W. H. Press, S. A. Teukolsky, W. T. Vetterling, and B. P. Flannery, *Numerical Recipes 3rd Edition: The Art of Scientific Computing* (Cambridge University, 2007).
38. M. Majic and E. Le Ru, "Basic codes to evaluate normalized spherical Bessel functions and logarithmic derivatives of the Riccati Bessel functions," figshare, 2019, https://doi.org/10.6084/m9.figshare.9937082, 10 March 2019.
39. M. I. Mishchenko, L. D. Travis, and A. A. Lacis, *Scattering, Absorption, and Emission of Light by Small Particles* (Cambridge University, 2002).